Diego Ribas Gomes

NANOSECOND ABLATION OF ALUMINA WITH AN YTTERBIUM FIBRE-LASER: EXPERIMENTAL STUDY, TOPOGRAPHY AND DAMAGE EVALUATION

Dissertação submetida ao Programa de Pós-Graduação em Ciência e Engenharia de Materiais para a obtenção do Grau de Mestre em Ciência e Engenharia de Materiais.
Orientador: Prof. Dr.-Ing. Márcio Celso Fredel
Universidade Federal de Santa Catarina
Supervisor: Dr.-Ing. Rolf Janssen
Technische Universität Hamburg-Harburg

Florianópolis

2014

Ficha de identificação da obra elaborada pelo autor,
através do Programa de Geração Automática da Biblioteca Universitária da UFSC.

Gomes, Diego Ribas
Nanosecond ablation of alumina with an ytterbium fibre-laser : Experimental study, topography and damage evaluation / Diego Ribas Gomes ; orientador, Márcio Celso Fredel - Florianópolis, SC, 2014.
75 p.

Dissertação (mestrado) - Universidade Federal de Santa Catarina, Centro Tecnológico. Programa de Pós-Graduação em Ciência e Engenharia de Materiais.

Inclui referências

1. Ciência e Engenharia de Materiais. 2. Laser-de-fibra. 3. Ablação. 4. Alumina. 5. Resistência. I. Fredel, Márcio Celso. II. Universidade Federal de Santa Catarina. Programa de Pós-Graduação em Ciência e Engenharia de Materiais. III. Título.

Diego Ribas Gomes

NANOSECOND ABLATION OF ALUMINA WITH AN YTTERBIUM FIBRE-LASER: EXPERIMENTAL STUDY, TOPOGRAPHY AND DAMAGE EVALUATION

Esta Dissertação foi julgada aprovada para a obtenção do Título de "Mestre em Ciência e Engenharia de Materiais", e aprovada em sua forma final pelo Programa de Pós-Graduação em Ciência e Engenharia de Materiais.

Florianópolis, 14 de março 2014.

Prof. Dr. Antônio Pedro Novaes de Oliveira
Universidade Federal de Santa Catarina
Coordenador

Banca Examinadora:

Prof. Dr.-Ing. Márcio Celso Fredel
Universidade Federal de Santa Catarina
Orientador

Prof. Dr.-Ing. Carlos Pérez Bergmann
Universidade Federal do Rio Grande do Sul

Prof. Hazim Ali Al-Qureshi, PhD
Universidade Federal de Santa Catarina

Prof. Dr.-Ing. Walter Lindolfo Weingaertner
Universidade Federal de Santa Catarina

This work's dedicated to the bright Son of the morning, who brings to light the hidden things of darkness

ACKNOWLEDGMENTS

My sincere thanks to:

the Federal University of Santa Catarina, my advisor prof. Dr.-Ing. Márcio Celso Fredel for the thorough attention and prof. Dr.-Ing. Dachamir Hotza for the excellent opportunity;

the Hamburg University of Technology and the Institute of Advanced Ceramics staff, especially Dr-Ing. Rolf Janssen, for all the support;

the Institute for Laser Systems and Process Technologies, specially Dipl.-Ing.oec. Sina Hallmann and Dipl.-Ing. Christian Daniel for the helpfulness and insightful discussions;

the Materials Science and Engineering Graduate Program (PGMAT) and the brazilian Coordination for the Improvement of Higher Education Personnel (CAPES), for the scholarships;

all teachers who seriously carry their roles of knowledge spreaders;

my institute colleagues, for all the professional as well as recreational moments;

my beloved Fernanda Coutinho Soares, for her presence.

(...) Hic est totius fortitudine fortitudo fortis; quia vincet omnem rem subtilem, omnemque solidam penetrabit. (...)

Tabula smaragdina Hermetis Trismegisti

RESUMO

A utilização de cerâmicas avançadas tem sido limitada pelos altos custo de usinagem, com desbaste e polimento correspondendo a 50-80% do custo total do produto final; e pela dificuldade em obter controle dimensional e qualidade de superfície satisfatórios. Processos ablativos com laser apresentam-se como alternativa, tendo em vista a ausência de ferramentas sujeitas a desgaste e a possibilidade de remover quantidades muito pequenas de material. Ainda que a pesquisa sobre ablação a laser seja um tópico de interesse atual, com um número crescente de publicações ano após ano, ela tem sido focada em pulsos ultra-curtos (na ordem de pico e femtosegundos), enquanto a pesquisa no regime de nanosegundos ($>$ 100 ns), de baixo custo e baixo consumo de energia, é relativamente escassa, especialmente para cerâmicas. Os resultados deste processo ainda são difíceis de se prever devido aos vários processos físicos simultâneos e auto-interativos que ocorrem em um tempo relativamente curto. Neste estudo, realizou-se uma análise experimental para um processo de usinagem tridimensional utilizando um laser de fibra de itérbio com pulsos de 120 ns, a princípio através de projeto de experimentos e, posteriormente, por um procedimento de otimização passo-a-passo, avaliando-se a taxa de remoção e rugosidade resultantes em amostras densas de alumina. Posteriormente, a morfologia da superfície e a resistência à fratura foram avaliadas para dois conjuntos "otimizados" de parâmetros. Observou-se uma diferença bem definida nas taxas de ablação e topografias resultantes, sugerindo a existência de um ponto limite entre mecanismos distintos de remoção. Uma das combinações deu origem a marcas de ondas-de-choque retas e com ângulo definido entre si, circundando poços de fusão. A resistência à fratura para os dois regimes também diferiu significativamente, com um aumento do módulo de Weibull (121,6% e 163,5%) associado a uma diminuição da tensão característica, em comparação às amostras não-usinadas.

Palavras-chave: Laser-de-fibra. Ablação. Alumina. Topologia. Resistência.

ABSTRACT

The use of advanced ceramics has been limited by the high machining costs, with grinding and polishing accounting for 50-80% of the final product's total cost; and the inability of achieving satisfactory dimensional control and surface quality. Laser ablative processes are an alternative, considering the absence of wear-subjected tools and the possibility of very fine material removal. Although the research on laser ablation is a current topic of interest, with growing number of publications year after year, it's been focusing mainly on ultra-short pulses (in the order of pico- and femtoseconds), while the research on the low-cost and low-energy-consuming nanosecond regime ($>$ 100 ns) is relatively scarce, specially for ceramics. This process outcomes are still difficult to predict, due to the many simultaneous and self-interacting physical processes that take place in a relatively short time. In this study, an experimental analysis has been carried out for a three-dimensional machining process with a 120 ns pulsed ytterbium fibre-laser on dense Al_2O_3 samples, initially through design of experiments, and later trough a step-by-step optimization procedure, evaluating ablation rate and resulting roughness. Then, surface morphology and fracture strength were evaluated for two of the "optimized" parameters sets. A very well-defined difference in removal rate and resulting surface topographies was observed, suggesting a threshold point between distinct ablation mechanisms. One of the combinations gave rise to interesting features of straight, angled shock-waves around melt pits. The fracture strength for both regimes also differed significantly, with a clear increase (121,6% e 163,5%) of the Weibull modulus combined with a decrease of the characteristic stress, compared to the non-ablated samples.

Keywords: Fibre-laser. Ablation. Alumina. Topology. Strength.

LIST OF FIGURES

LIST OF TABLES

LIST OF ABBREVIATIONS AND ACRONYMS

LIST OF SYMBOLS

CONTENTS

1 INTRODUCTION

The advantages of lasers in materials processing, such as high achievable accuracies, cleanliness and absence of wear-subjected tools, combined with the ability of building compact, high performance and increasingly cheaper laser systems, have already been considered to suggest that after the technological ages of steam and electricity, we have now entered the age of photons. (MEIJER et al., 2002). The advent of very short laser pulses able to deliver high power with little energy to a material's surface has brought interest to the ablation process. The material responds to the high energy rates by spallation or evaporation, leaving little heat-affected zones, and hence little mechanical damage (STEEN; MAZUMDER, 2010).

Laser ablation can be used for several applications in manufacturing processes of metals, polymers, ceramics and composites, and an increasing number of publications on the theme have been released in the past few years (Fig. 1.). It is a specially attractive topic for advanced ceramics, since their use in large scale technological applications is limited by their high machining costs, that may account for between 50 and 80% of the final product cost (JAHANMIR; RUMULU; KOSHY, 1999; DAHOTRE; HARIMKAR, 2008; MARINESCU; D., 2012).

Figure 1 – Number of citations of the term "laser ablation" in the field "Science/Technology", in the period from 2009 to 2013.

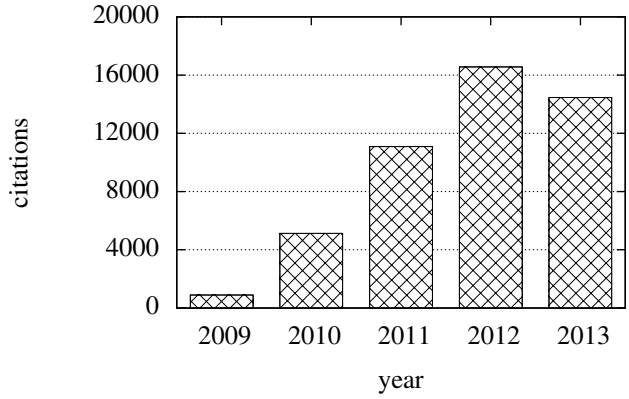

Source: Web of Knowledge database, acessed in 08/10/13.

Laser operations are already widespread in industry, in processes of casting, forming and joining, as well as one- (drilling) and two-dimensional (cutting) machining (DAHOTRE; HARIMKAR, 2008), due to their efficiency and economy. However, since ablation is a complex process governed by many interacting physical phenomena that depend on properties that evolve during the process, it is difficult to directly translate process parameters into desired effects such as removal depth and surface roughness or morphology (KNOWLES et al., 2007). Studies have been carried regarding parameters optimization (CAMPANELLI et al., 2007; WANG et al., 2008; KIBRIA; DOLOI; BHATTACHARYYA, 2010, 2013), and numerical models were developed regarding thermal processes (CHICHKOV et al., 1996; GUSAROV; SMUROV, 2005; CHIVEL; PETRUSHINA; SMUROV, 2007; YAN et al., 2011; YEO et al., 2012) and plasma dynamics (ZHOU et al., 2011; AMORUSO et al., 1999; CIRISAN et al., 2011; WU et al., 2013). Samant and Dahotre (2009) developed a comprehensive model for one-dimensional machining of ceramics, being able to predict removed depth from laser parameters and material properties; Vora et al. (2012) modeled the evolution of surface quality. Three-dimensional machining, however, is not fully developed and still has limited industrial use, requiring further research efforts (WANG; ZENG, 2007; DUBEY; YADAVA, 2008; DAHOTRE; HARIMKAR, 2008). Besides that, there are no quantitative studies on the effect of laser-ablative processes on the mechanical properties of ceramics.

In this context, the present study reports an experimental analysis of three-dimensional machining of alumina through ablation with a nanosecond pulsed laser, evaluating its practical feasibility regarding ablation rate, surface quality and loss of strength, and providing data for future numerical models.

1.1 OBJECTIVES

The present study aims to contribute into the relative gap in literature regarding the influence of the laser ablation process on the mechanical properties of ceramics, specifically on the fracture strength of alumina, as well as to increase the understanding of the underlying mechanisms and phenomena. In order to achieve this, the following specific goals are proposed:

- To produce alumina flexural-test samples with high density and small grain size, through pressing and sintering;

- To characterize and optimize the ablation process for the available nanosecond laser equipment;

- To evaluate the surface morphology and fracture strenght of the laser-ablated samples, in comparison to the original samples.

2 THEORETICAL BACKGROUND

2.1 LASER FUNDAMENTALS

Laser is an acronym for Light Amplification due to Stimulated Emission of Radiation. Although the first working ruby laser has been constructed by Theodor Maiman in 1960, it is based on a phenomenon predicted by Albert Einstein using a mathematical argument in 1917 (he postulated that a photon of radiation, when striking an excited species, would cause it to drop to a lower energy state, and emit a photon that would be in phase and traveling in the same direction as the initial striking photon). So to allow this stimulated emission to be amplified, instead of being absorbed, the active medium must have the capability of undergoing population inversion, that is, staying in such state where there are more excited molecules than lower-energy ones. This condition means that the lifetime of the excited species must be longer than the one of the lower-energy state for a given active medium material. By placing the active medium inside a resonant cavity with a set of mirrors and subjecting it to population inversion, the laser light can be amplified and sustained, generating a high-intensity laser beam output from one of the mirrors. A few properties of the laser beam are discussed below.

2.1.1 Laser beam characteristics

2.1.1.1 Wavelength

The laser radiation is one of the purest spectral forms of radiation available, due to the well defined energy transitions that generate the beam. Besides the characteristic of the material energy levels, virtually any wavelength between 0,01 μm and 1 mm can be produced using techniques of frequency implementation (doubling, tripling, etc.) or tunable lasers (STEEN; MAZUMDER, 2010). A few wavelengths for some important materials processing lasers are shown in Table 1.

2.1.1.2 Coherence

Coherence is the measure of orderliness of the waves, being composed by spatial (correlating the different points in space for a given moment in

Table 1 – Photon properties of different lasers.

Device	Wavelength, λ [μm]	Energy, E [eV]
Cyclotron	0,1 (X-ray)	12,3
Excimer laser	0,249 (UV)	4,9
Nd:YAG laser	1,06 (IR)	1,16
CO_2 laser	10,6	0,12

Source: Adapted from (STEEN; MAZUMDER, 2010)

time) and temporal coherence (correlating the phases in a given point in space for a period of time), as depicted in Fig. 2. Although this property allows for some very interesting applications, such as length gauging, speckle interferometry, holography and Doppler velocity measurements, it has not yet been used in materials processing. Steen and Mazumder (2010) suggest that future research could be developed so to use it as a penetration- meter or a mean of carrying out subtle experiments with interference-banded heat sources.

Figure 2 – Illustration of: a) spatially and temporally coherent radiation; and b) random radiation.

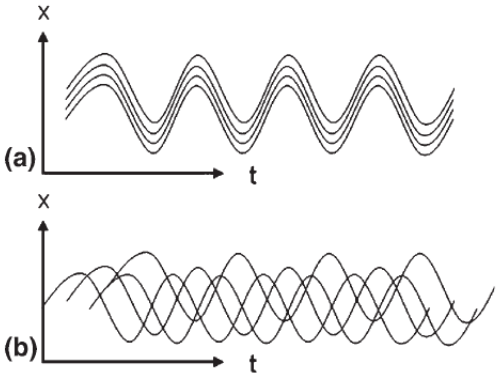

Source: (DAHOTRE; HARIMKAR, 2008).

2.1.1.3 Transverse modes and spot size

Inside the laser cavity, according to its geometry, there are standing electromagnetic waves at slightly different angles, during the optical oscilla-

tion. The interference between these waves give a transverse standing wave that emerges from the cavity as the mode structure of the beam. They are represented by TEM_{mn}, where m and n are integers representing the number of nodes in the direction perpendicular to that of the beam. Some of these modes can be seen on Fig. 3.

Figure 3 – Some beam transverse modes.

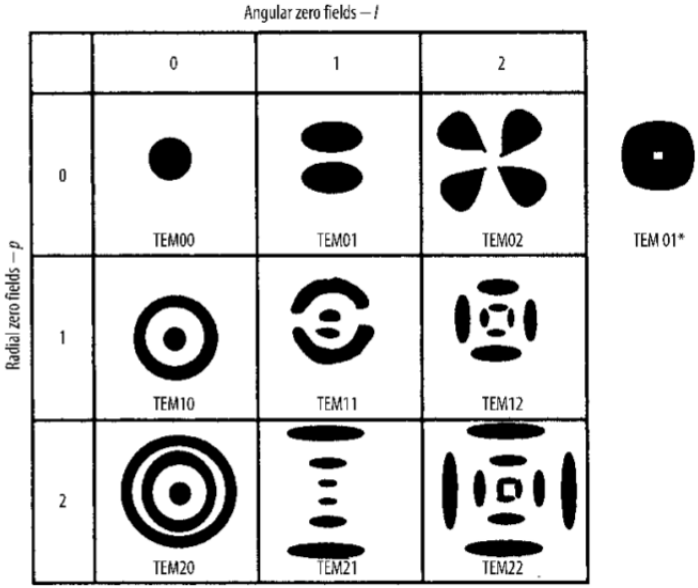

Source: (STEEN; MAZUMDER, 2010).

The most used mode for laser machining applications is the TEM_{00}, which has a Gaussian spatial distribution (Fig. 4). This intensity distribution can be expressed as:

$$I(r) = I_0 exp[\frac{-2r^2}{w_e^2}] \tag{2.1}$$

where r is the distance from the beam center, I_0 is the intensity at r = 0, and w_e is the spot size, defined as the distance from the beam axis where the intensity drops to e^{-2} (13,5 %) of the value at the beam center.

Figure 4 – Intensity distribution for some transverse modes.

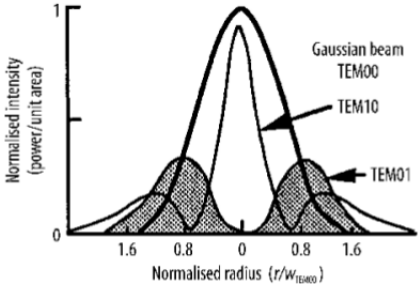

Source: (STEEN; MAZUMDER, 2010).

2.1.1.4 Temporal modes

A laser output can be either continuous, with a constant amplitude, when it is called continuous wave (CW) mode; or pulsed, when the energy is stored up to a certain level, and discharged in a short, high energy pulse. An important parameter for pulsed mode is then the frequency, or pulse repetition rate (F_r). The lower is the frequency, the longer the inter-pulse interval will be, meaning that the equipment will be able to store more energy before the discharge, hence achieving a higher pulse peak power (P_p). The peak power can be expressed as:

$$P_p = \frac{P}{\tau_l F_r} \tag{2.2}$$

where P is the average output power provided by the equipment and τ_l is the pulse duration. Shorter pulses allow higher rates of energy discharge, therefore higher peak powers.

2.1.2 Laser types

Lasers can be classified according to different characteristics, and it is common to divide them by the physical state of the laser material (EICHLER; EICHLER, 2010), as:

- Solid-state lasers;
- Liquid lasers;

- Gas lasers; and
- Free-electron lasers.

Solid-state lasers have higher mechanical stability and work-life than liquid and gas lasers, due to the absence of leaking risks; and can be pumped by simple diode-lasers, allowing for compact and efficient systems.

2.1.2.1 Fibre-lasers

Glass-structured laser media can be pulled into thin fibres, which can be diode-pumped through one of its ends, producing the laser radiation inside the fibre. The advantages related to this configuration are the excellent achievable beam qualities (due to the fibre's high aspect ratio) and good thermal transport associated with the large fibre's surface, making this kind of lasers not dependent on additional cooling systems.

Double-clad fibres have a core of active laser medium with high refractive index, surrounded by an inner cladding with lower index which guides the pump light through the fibre, and an outer cladding, or jacket, made usually of a polymer material (Fig. 5). The inner clad is made not perfectly round, so that all pump-light rays cross the active core, making it possible to achieve higher powers with near diffraction-limited beam quality (EICHLER; EICHLER, 2010).

Figure 5 – Double-clad fibre-laser scheme.

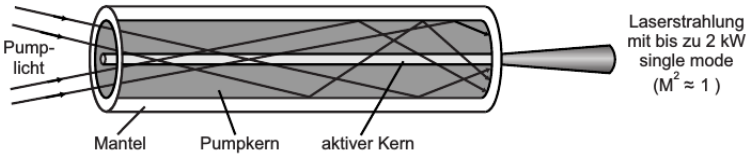

Source: (EICHLER; EICHLER, 2010).

2.2 LASER ABLATION

Laser ablation processes have become important since the possibility of achieving short pulses with very high power has been attained. Given these characteristics, it is possible to get fine material removal with very a little thermally affected zone. Besides that, when compared to conventional

machining processes, laser ablation is clean and not subjected to tool wear. Some of its applications include the texturing of hard disks, silicon wafer marking, microelectronic trimming, inkjet printer head drilling and medical devices manufacture (KNOWLES et al., 2007).

2.2.1 Laser-material interactions

When an electromagnetic radiation strikes a given surface, it undergoes different phenomena such as reflection, absorption, refracting, scattering and transmission (Fig. 6). The amount of each phenomenon is going to be a function of both radiation and material properties. Most of materials processing applications are based on absorption of laser energy and subsequent transformations such as heating, melting, vaporizing and plasma formation. The absorption of the radiation intensity can be generally expressed as the Beer-Lambert law:

Figure 6 – Phenomena decurring from light-matter interaction.

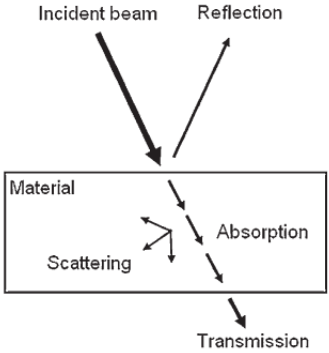

Source: (DAHOTRE; HARIMKAR, 2008).

$$I(z) = I_0 e^{-\alpha z} \tag{2.3}$$

where z is the distance that radiation has traveled inside the material and α is the materials absorption coefficient, which is a function of temperature, as well as the radiation's wavelength and intensity. The optical penetration length, over which the beam is significantly attenuated, is defined as the inverse of the absorption coefficient:

$$l_\alpha = \alpha^{-1} \tag{2.4}$$

Considering that the electromagnetic wave has an electrical field component, it is going to subject any charges it meets to a certain force. In the case of a solid substrate, some elementary excitations that are optically active, besides electronic excitations, are those of phonons, polaritons, magnons, etc (Fig. 7); and also localized electronic or vibrational states related to defects, impurities, or the solid surface itself. The absorption of photon energy by electrons happens through a phenomenon called inverse Bremsstrahlung, that is, the photon energy is absorbed as an increase in the electron's kinetic energy. These high-energy electrons will either re-radiate in all directions, or be constrained by the phonons structure, in the form of lattice vibration, meaning that the energy has been absorbed (since it no longer radiates) in the form of heat (FAN; LONGTIN, 2001). The time of interband electronic excitations τ_e is typically in the order of 10^{-13} seconds for metals and 10^{-12} to 10^{-6} for non-metals, while electron-phonon relaxation times, τ_i, are usually longer (in the order of picoseconds), due to the difference between electrons and ions masses. So, the absorption of radiation energy and the dissipation through the structure is going to define the temperature distributions inside the bulk. The extent to which this heat is absorbed can lead to melting, vaporizing, and to plasma formation through the ionization of the vapor. Pulse lengths are classified as 'ultra-short' when the distance by which heat diffuses during the irradiation is smaller than the optical penetration depth; and as short, otherwise. For ceramics, ultra-short pulses are typically shorter than 10 ps (MEIJER et al., 2002).

In the case that the energy of the photon is high enough, it can directly break the atoms bonds (photo-decomposition), without heating. This kind of non-thermal modification is called photochemical processing. However, even if one bonds is broken by the inciding photons, they would very quickly form again, except for the case when a big amount of photons would strike the bonds at the same time, resulting in permanent damage. Taking the bond energy in Al_2O_3 as example, of 5,20 eV (LUO, 2010), and comparing to the photon energy of a 1064 nm wavelength laser, of 1,16 eV, shows that photolytic bond breaking would require 5 simultaneously inciding photons, meaning a very high radiant exposure (hereafter referred to as fluence).

In the case of low laser-induced excitation rate, though, the absorbed energy can be considered as being directly transformed into heat, allowing the material response to be treated in a purely thermal way. Pulsed laser processing in the nanosecond regime is typically characterized by photothermal mechanisms (BROWN; ARNOLD, 2010). The heat diffusion length, or the distance over which temperature changes propagate during a certain time (in this case, the pulse length τ_l), is given by

Figure 7 – Scheme of different kinds of electronic excitations in solids.

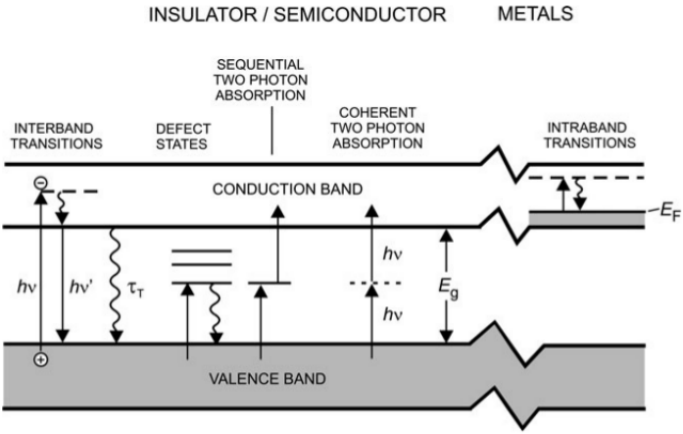

Wavy arrows are non-radiative processes, opposed to straight arrows. VB $\rightarrow$ CB transitions occur when the photon energy is higher than the bond energy. Source: (BÄUERLE, 2011).

$$l_t \approx 2(D\tau_l)^{\frac{1}{2}}, \tag{2.5}$$

where D is the material's thermal diffusivity. The dimensionality of the heat flow inside the material is then characterized by the relations between this l_t and other characteristic sizes as the optical penetration length l_α and the focal spot size w_e. In the case when $l_t >> l_\alpha, w_e$, one must consider the 3-dimensional heat propagation. For the case when $l_\alpha \leq l_t$ and $l_t << w_e$, lateral heat propagation can be ignored and the temperature distribution in z direction can be obtained by the single dimension heat equation (BÄUERLE, 2011).

2.2.2 Nanosecond laser ablation

The important factors that are going to define the ablation process are the times of electron cooling τ_e, lattice heating τ_i and pulse duration τ_l (PHAM; DIMOV; PETKOV, 2007). For nanosecond pulses, the relation between these times is $\tau_e < \tau_i < \tau_l$, which means that the energy is absorbed by the material and is converted into heat, leading to melting and vaporization, while the radiation is still propagating into the structure. Given the relatively

long time heat has to propagate, evaporation occurs from a large layer of molten material, which impairs the precision of the process (CHICHKOV et al., 1996). It also gives time for the vaporized material to absorb the radiation and form a plasma plume, that is maintained during the pulse duration and absorbs and defocuses the beam energy, causing a higher intensity requirement for deeper penetration. These characteristics lead to secondary effects such as a heat affected zone (HAZ), microcracks, surface damage due to shockwave and debris from ejected material (Fig. 8).

Figure 8 – Laser ablation scheme for nanosecond and longer pulses.

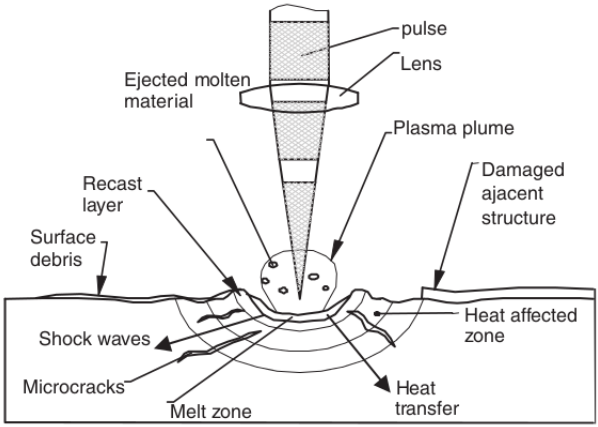

Source: (PHAM; DIMOV; PETKOV, 2007).

In order to machine tridimensional structures, the ablation process consists of overlapping pulses to form a line or track, and combining the tracks to fill the desired shape. A scheme of the process is shown in Fig. 9. The speed in which the pulses advance to form the ablated lines is referred to as scan speed, V_s, and the lateral distance between lines as track distance, S_a. The process can be repeated a number n of times, repeating layers of ablation to achieve the desired depth.

Figure 9 – Scheme of the ablation process: a) pulse; b) track; c) shape.

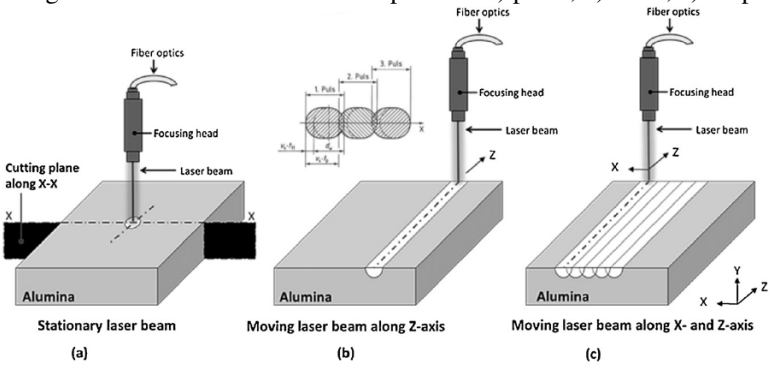

Source: adapted from (VORA et al., 2012) and (DIN 32540).

2.2.2.1 Fluence threshold

For pulsed lasers, the fluence of a single-mode beam, or its radiant exposure (energy per unit area) can be obtained from:

$$\phi = \frac{Q}{\pi w_e^2}, \tag{2.6}$$

where Q is the average energy output (JR., 2009).

Significant material removal occurs only above a threshold fluence, which is determined by both material's characteristics, such as microstructure, morphology and density of defects; and laser parameters as wavelength and pulse duration. Gusarov and Smurov (2005) have proposed a thermal model for nanosecond laser ablation, and explained the threshold fluence as the point where 100 % of the laser energy is being spent on heating the target; for fluences above the threshold a fraction of the energy is spent on overcoming the condensed state binding energies, resulting in evaporation.

Because the size of a given ablated spot is always going to be smaller than that of the incident beam, due to the latter's Gaussian intensity profile, eq. 2.1 can be rewritten as:

$$I_{th} = Ie^{\frac{-2r_a^2}{w_e^2}} \tag{2.7}$$

where I_{th} is the ablation intensity threshold and r_a is the ablated radius. Rearranging eq. 2.7 for the ablated diameter D_a, one comes to

$$D_a^2 = 2w_e^2[ln(I) - ln(I_{th})] = 2w_e^2[ln(P_p) - ln(P_{p,th})] \tag{2.8}$$

where $P_{p,th}$ is the ablation threshold peak power, whose use here has the advantage of not being dependent on the focal spot size, still unknown. When the track's width and incident peak power are known, eq. 2.8 allows to estimate beam radius and threshold peak power, since these are constant (BÄUERLE, 2011).

By combining Beer-Lambert law (eq. 2.3) and Gaussian intensity distribution (eq. 2.1) equations, and taking into account that the ablated depth $h_a(r)$ is going to be determined by the depth where the laser intensity reaches the threshold point, one can write:

$$I_{th}(r,z) = Ie^{\frac{2r^2}{w_e^2}} e^{-\alpha h_a(r)} \tag{2.9}$$

which, rearranged for the ablation depth, gives:

$$h_a(r) = \frac{ln(I/I_{th}) - \frac{2r^2}{w_e^2}}{\alpha} \tag{2.10}$$

As each ablated line consists on a series of overlapping pulses, one can consider the total track depth H_t as:

$$H_t = Nh_a(0)C_c = \frac{W_t F}{V} h_a(0) C_c \tag{2.11}$$

where N is the number of repeated pulses over each spot, $h_a(0)$ is the single pulse removal depth, and C_c is a correction coefficient, due to the non-flat profile of the ablated tracks (WANG et al., 2008). This correction coefficient can be calculated as:

$$C_c = \frac{\sum_1^N h_a(r)}{Nh_a(0)} \approx \frac{\int_{\frac{-W_t}{2}}^{\frac{W_t}{2}} h_a(r)dr}{W_t h_a(0)} = 1 - \frac{W_t^2}{6w_e^2 ln(I/I_t h)} \tag{2.12}$$

By these means, it is possible to calculate the single-pulse ablation depth using the measured track's width and depth.

2.3 CERAMICS

2.3.1 Alumina

Aluminium oxide (Al_2O_3), or alumina, is the most widely used ceramic oxide. It occurs naturally as the mineral corundum, popularly known as the precious stones sapphire and ruby, when doped with trace amounts of impurities such as iron, titanium, chromium, copper, or magnesium. Large scale production of alumina powder is achieved by refining the mineral bauxite, which is a mixture of the minerals boehmite (α-AlO(OH)), diaspore (β-AlO(OH)) and gibbsite ($Al(OH)_3$), with a high content of impurities as Na_2O, SiO_2, TiO_2 and Fe_2O_3 (RIEDEL; CHEN, 2011). The Bayer process involves selective leaching of the aluminium oxide by caustic soda, followed by precipitation of the purified, fine-particle-size aluminium hydroxide and thermal conversion to Al_2O_3 powder (RICHERSON, 2005). Pure nanopowders, due to their low-temperature sinterability, high chemical reactivity and enhanced plasticity, are required for the preparation of submicrometer-grained alumina (RIEDEL; CHEN, 2011).

A great deal of information is available on alumina's raw materials production, its sintering behaviour and sintered product properties, and it is often used as an example in ceramic technology textbooks and for development purposes (SALMANG; SCHOLZE, 2007). Its applications range from engineering to the biomedical field: ignition plugs, tap washers, pump seals, electronic substrates, grinding media, abrasion-resistant tiles, cutting tools, body armors, laboratory gear, orthopedic and dental applications, among many others.

2.3.2 Strength evaluation

Ceramic materials are prone to brittle fracture, i.e. without prior measurable plastic deformation. Observed values of strength measurements are usually associated with a certain scatter, which is related to the distribution of size, orientation and position of defects in the material's bulk.

The weakest link theory is based on the idea that the propagation of any existing flaw will ultimately lead to the sample's total failure, and that the flaws are homogeneously distributed over the volume. In order to describe the strength distribution of ceramic samples, the Weibull experimental approach is usually used, allowing for prediction of failure probability for any applied stress (GREEN, 1998).

The distribution is given by

$$P_f(\sigma) = 1 - exp\left[-\left(\frac{\sigma}{\sigma_0}\right)^m\right] \tag{2.13}$$

where P_f is the cumulative probability of fracture being caused by a stress σ; m is the Weibull modulus, an inverse measure of the distribution width; and σ_0 is a measure of centrality, called characteristic stress, and represents the point at which the probability of fracture is 0,63 (WACHTMAN; CANNON; MATTHEWSON, 2009).

It has been shown (JAYATILAKA; TRUSTRUM, 1977) that a Weibull distribution occurs for homogeneous materials under homogeneous tension, and flaw populations with relative frequencies $g(a)$ that decrease by a negative power of their effective size a:

$$g(a) = g_0\left(\frac{a}{a_0}\right)^{-r} \tag{2.14}$$

and r is related to the Weibull modulus m by:

$$m = 2(r-1). \tag{2.15}$$

Although the Weibull distribution function has been the basis of the mechanical design of ceramic components, its assumption of non-interacting flaws, posed by the weakest link theory, is questioned when very small flaws are the origin of fracture, since the flaw density associated with them would be too high for them not to interact; and also for very small specimens, as the flaw density should be lower than the predicted (DANZER, 2006). These considerations are only significant for samples with effective volume of the order of 10^{-4} mm^{-3} (e.g. for microelectronic devices), which would require a new statistical theory of brittle fracture.

2.3.3 Laser damage in ceramics

Ceramics are prone to crack formation due to the thermal stresses induced by the laser ablation process in the nanosecond regime. For this pulse-length range, Knowles et al. (2007) have pointed out that the processing strategy that allow for minimum damage is to keep a low thermal input to the bulk, basically by avoiding the formation of an intense plasma, since it radiates heat into the material for a period usually much longer than the pulse duration, as Zhou et al. (2011) have observed through time-resolved observations of nanosecond ablation on silicon. The plasma formation is mainly

affected by the intensity of the laser, so it should be kept at an optimized level where there is a compromise between removed volume and plasma formation. Their conclusion is in agreement with the work of Yeo et al. (2012), where the residual stress changes in Al_2O_3 due to Nd:YAG laser irradiation have been studied through x-ray diffraction and the tensile residual stresses were found to increase in proportion to the energy density. A three-dimensional finite element model for simulation of laser cutting of Al_2O_3 has been developed by Yan et al. (2011), and their study also concluded that modest peak powers would be preferable for single-pass crack-free cutting.

For pico- and femtosecond range (called ultrashort), due to different mechanisms leading to ablation, such as desorption of excited species from the surface, non-equilibrium effects related to electronic and vibrational excitations, Couloumb explosion, etc; the kind of damage is also diverse. Ashkenasi, Stoian and Rosenfeld (2000) have studied the ablation behavior of alumina under this pulse length range, and have found that bulk damage is generated with fluences below the threshold, due to beam narrowing effect. It would also be reasonable to expect some defect formation in the nanosecond regime, since the very large temperature gradients that can be achieved below the melt and/or vaporizing threshold could induce thermal stresses and thermoelastic excitation of acoustic waves, contributing to effects such as work hardening, warping or cracking. Chivel, Petrushina and Smurov (2007) have simulated nanosecond ablation of metals with high melting point, finding that the gas contained in micro- and nano- sized pores below the surface can be heated due to the laser irradiation and the pressure can result in surface destruction below the evaporation threshold.

3 METHODOLOGY

The experiments are separated in two main groups, the first concerning the characterization and optimization of the ablation process, which was based on the methodology reported in Campanelli et al. (2007), Wang et al. (2008), Kim, Sohn and Jeong (2009); and the second concerning the actual research point of interest: the kinds of morphologies that rise from two different set of laser parameters and their effect on the stress fracture.

3.1 MATERIALS AND EQUIPMENTS

Ceramic bars have been produced by uniaxially pressing the Al_2O_3 powder (TAIMEI TM-DAR) with 100 MPa, followed by isostatic pressing with 400 MPa. Afterwards the green bodies were sintered at 1350°C, with a dwell time of one hour, and heating/cooling rate of 10°C/min. The sintered pieces were then cut and ground to the final dimensions of 2 $\times$ 2,5 $\times$ 3,5 mm $\pm$ 0,2 mm, and one of the surfaces was polished down to a grit size of 0,25 μm. The density of the samples was determined to be 99,8% of Al_2O_3 theoretical density, using the Archimedes method.

The ablation experiments have been conducted using a pulsed ytterbium fiber-laser (1064 nm wavelength) with 200W maximum average power output, using pulse time of 120 ns and focal length of 163 mm, in normal atmosphere and pressure conditions. The main parameters in the present three-dimensional laser machining system (Fig. 10) are a) the pumping current, which is directly related to the pulse energy; b) the frequency or repetition rate F_r, which together with the pumping current, defines the average power output and the beam's fluence; c) the track distance (S_a), or the spacing between each of the lines that forms the desired bi-dimensional feature on the samples surface; and d) the scan speed (V_s), the speed at which the beam advances to ablate each track. The number of layers also plays an important role, since they determine the final depth, but they have been kept out of the present study in order to avoid the complexity introduced by multi-pulse enhancement (FU et al., 2010), which are beyond the proposed scope.

The ablated features such as depth and roughness were measured using a Keyence VK-X100 laser scanning microscope (LSM). Its optical profilometer has a resolution of 5 nm and the advantage of not depending on a probe tip's size, like other contact methods such as atomic force microscopy. Values for roughness refer to the R_a value, that is, the average value of the distance between each point's position to the surface overall average line. A LEO 1530

Figure 10 – Schematic diagram of the laser system.

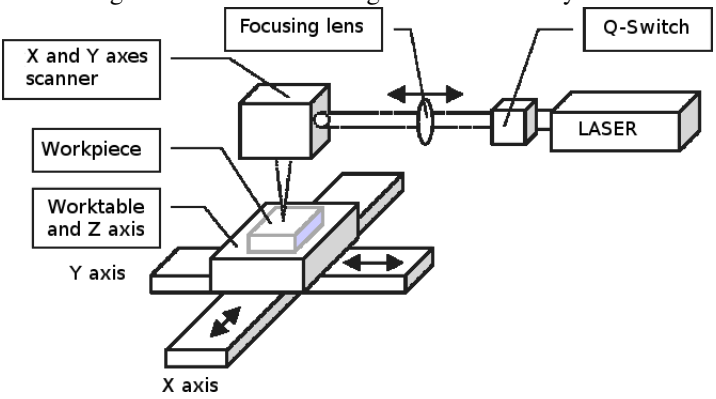

Source: adapted from (PHAM et al., 2004).

scanning electron microscope (SEM) was also used to qualitatively evaluate the ablated surfaces.

3.1.1 Notation

In order to make it easier to refer to the various sets used for the different experiments, they were named as:

$$\underbrace{XX}_{\text{experiment identification}} \quad \phi \quad \underbrace{YY}_{\text{fluence in J/cm}^2} \quad ,$$

e.g. $TD\phi 30$ refers to the set of the track distance (TD) evaluation with fluence of 30 J/cm^2.

3.2 EXPERIMENTAL PROCEDURE

3.2.1 Response surface statistical investigation

The first attempt to grasp the effects of pumping current, frequency, scan speed and track distance in the removal rates and resulting surface roughnesses was made through a central composite, full factorial response surface statistical design. Each of the 31 base runs for such design was replicated,

giving a total of 62 collected data points. The levels used for each one of the factors are listed on Table 2.

Table 2 – Values of the factors levels in the statistical design.

Level	-2	-1	0	1	2
Pumping current [%]	20	38	55	73	90
Frequency [kHz]	10	33	55	78	100
Scan speed [mm/s]	500	1250	2000	2750	3500
Track distance [μm]	15	24	33	41	50

Each combination of the design was used to ablate squares of 4 $\times$ 4 mm^2 on the polished surface of the samples, with 25 layers of removal. The ablation depth and the roughness of the resulting surface were measured with the LSM.

3.2.2 Reproducibility of outcomes

In order to evaluate the precision of the ablation process, three parameter sets were picked based on the ones previously used in the statistical design, according to a logic of low, medium and high fluences. These parameters are listed on Tab. 3.

Table 3 – Parameters combinations for the reproducibility evaluation.

Set name	Rϕ23	Rϕ33	Rϕ43
Pumping current [%]	38	55	73
Frequency [kHz]	33	55	78
Scan speed [mm/s]	1250	2000	2750
Track distance [μm]	24	33	24
Fluence [J/cm^2]	23	33	43

For each set, ten squares of 5 $\times$ 5 mm^2 were ablated in random order, using five alumina samples (six squares per sample). The depth of these squares and their roughness were measured using the LSM. Optical images were taken with a microscope to qualitatively evaluate the resulting effects.

3.2.3 Threshold investigations

For the threshold investigations, single tracks were ablated on the samples surface with increasing pumping currents from 30 to 80%, while keeping the frequency (25 kHz), for two different scan speeds (150 and 300 mm/s). Each of the twelve combinations was repeated 5 times. The width and depth of the tracks were measured using the LSM, and the averages for each set of parameters were used to calculate the focal spot size, intensity/fluence threshold and single-pulse ablation depth according to eq 2.8 and 2.10.

3.2.4 Track distance investigations

In order to find the most adequate track distances, squares with 4 $\times$ 4 mm were ablated on the samples' polished surfaces by combining parallel tracks, with distances varying from 4 to 16 μm, and the ablated regions' height profiles were measured using the LSM. Two further experiments were made for smaller and higher pump currents, namely 40% and 70%, to evaluate whether the optimal track distance could be a fixed ratio of the pulse size. In the latter case, the chosen values for track distance were such that would allow similar overlapping (from 10 to 22 μm), due to the considerably bigger ablated spot size. For all three sets, a step of 2 μm was used. Frequency (25 kHz) and scan speed (150 mm/s) were kept constant for three different fluences, which are shown in Tab. 4.

Table 4 – Parameters combinations for the track distances evaluation.

Set name	TDϕ24	TDϕ30	TDϕ42
Pumping current [%]	40	50	70
Track distance [μm]	6;8;10;12;14;16		10;12;14;16;18;20
Fluence [J/cm^2]	24	30	42

3.2.5 Scan speed investigations

Three parameter combinations were chosen to ablate squares with 50 layers of removal, whose depths were then measured and used to calculate the ablation rate A_r as:

$$A_r = \frac{h_a V_s S_a}{n} \tag{3.1}$$

where h_a is the ablated depth and n is the number of ablation layers. Track distance was kept constant at 10 μm, remaining parameters are listed on Tab. 5. Each combination was repeated 5 times and the average was considered for the calculation.

Table 5 – Parameters combinations for the scan speed evaluation.

Set name	SSϕ30	SSϕ36	SSϕ42
Pumping current[%]	50	60	70
Frequency [kHz]	25	20	20
Scan speed [mm/s]	50;100;150;200;300;400		
Fluence [J/cm^2]	30	36	42

3.2.6 Fracture strength evaluation

The parameter combinations with highest ablation rate within the sets SSϕ36 and SSϕ42, shown on tab. 6, were chosen to the fracture strength evaluation, as well as a polished, non-ablated control group. Each group consisted of 36 samples.

Table 6 – Parameters combinations for the fracture stress evaluation.

Set name	Wϕ00	Wϕ36	Wϕ42
Pumping current [%]	–	60	70
Scan speed [mm/s]	–	300	100
Fluence [J/cm^2]	–	36	42

These parameters were used to ablate a rectangle on the central region of the bending-test specimens, so that the whole surface between the rollers was processed. These samples were subjected to four-point flexure test according to (DIN EN 658-3), with support and loading spans of 20 and 10 mm, respectively. Stresses were calculated by the formula:

$$\sigma_{4,20} = \frac{3FL}{4bd^2} \tag{3.2}$$

where the subscripts refer to the number of supports and outer span length, F is the break force, L is the outer span, b is the samples width and d is the samples height; the probability of fracture P_f was assigned by:

$$P_f = \frac{i - 0,5}{X} \tag{3.3}$$

where i is the ascending rank of each datum with respect to the stress values and X is the total number of samples. This probability assignment formulation was chosen due to its wide use and negligible bias (QUINN; QUINN, 2010; WACHTMAN; CANNON; MATTHEWSON, 2009).

Critical defect sizes $a_{c,i}$ were attributed to the fracture strength values σ_i according to the Griffith/Irwin criterion:

$$a_{c,i} = \frac{1}{\pi}\left(\frac{K_{Ic}}{Y\sigma_i}\right)^2 \tag{3.4}$$

by setting the fracture toughness K_{Ic} to 3,4 $MPam^{1/2}$ (MORRELL, 2006; YAO et al., 2011) and the defect geometric factor Y to $\pi/2$, for volume penny-shaped cracks. The frequency distribution density of flaw sizes $g(a_{c,i})$ was calculated using the formula (DANZER, 2006):

$$g(a_{c,i}) = \frac{r-1}{V_{eff}a_{c,i}} ln \frac{2X}{2X - 2i + 1} \tag{3.5}$$

where V_{eff} is the effective volume for the four-point bending test, calculated as (MUNZ; FETT, 1999):

$$V_{eff} = \frac{Lbd}{2(m+1)} \tag{3.6}$$

and r is the exponent describing the decrease of the density of the flaw population's relative frequency according to flaw size.

4 RESULTS

4.1 PARAMETERS MAIN EFFECTS

The response surface method proved itself not adequate, giving a significant lack of fit. Nonetheless, the measured responses give an overall idea of the process behaviour for the tested ranges. The main effects plots in Fig. 11 and 12 show the average value of the measured responses for all data points at each given level of the factors, as well as their standard deviations.

Figure 11 – Main effects plot for total depth of ablation: a) pump current; b) frequency; c) scan speed; and d) track distance.

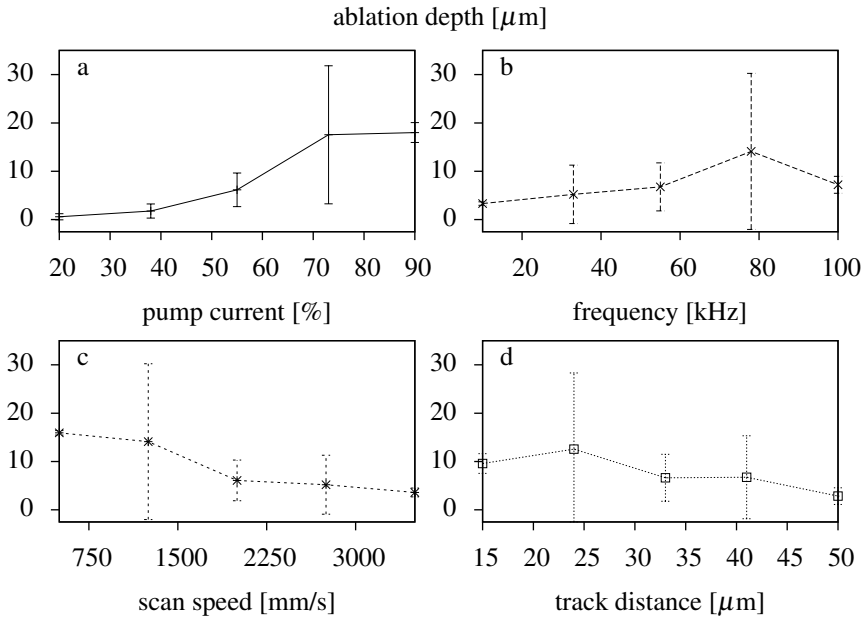

Figure 12 – Main effects plot for surface roughness (R_a): a) pump current; b) frequency; c) scan speed; and d) track distance.

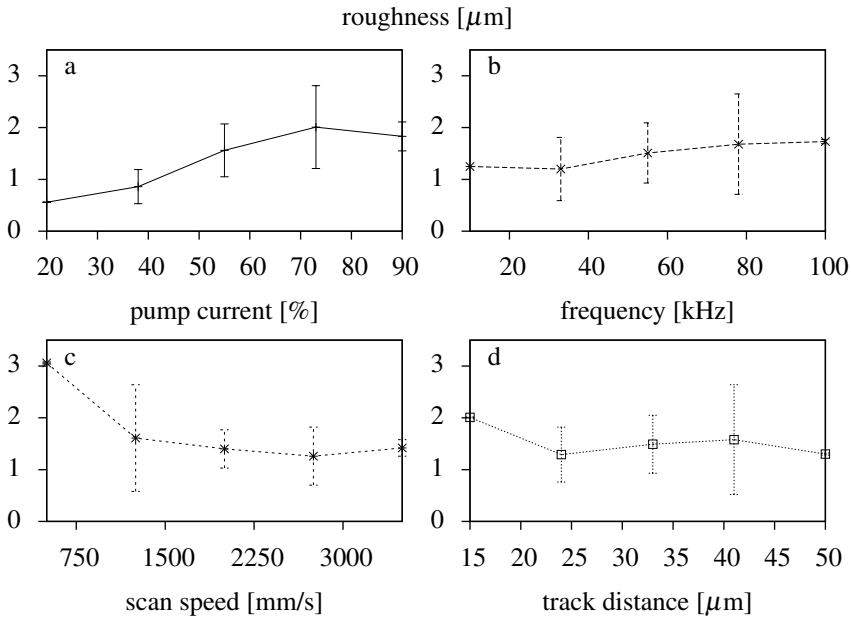

4.2 REPRODUCIBILITY

A resume of the measured values for ablation depth and roughness is presented in Tab. 7 and additionally in Fig. 13. The optical images of the ablated features, taken with the LSM, are also of interest as they show very distinct effects on the surrounding, not-ablated surface (Fig 14).

Table 7 – Descriptive statistics of reproducibility experiment for ablation depth.

Set name	Rϕ23	Rϕ33	Rϕ43
Number of measurements		10	
Depth			
Mean [μm]	3,295	9,755	27,79
Standard deviation [μm]	2,255	2,790	3,490
Coefficient of variance [%]	68,48	28,60	12,55
Range (max - min) [μm]	7,660	7,890	10,24
Roughness			
Mean [μm]	1,145	2,985	4,800
Standard deviation [μm]	0,293	0,139	0,915
Coefficient of variance [%]	25,58	4,66	19,02
Range (max - min) [μm]	0,900	0,460	3,400

Figure 13 – Results of ten measurements for ablated depth and roughness: a) Rϕ23; b) Rϕ33; c) Rϕ43.

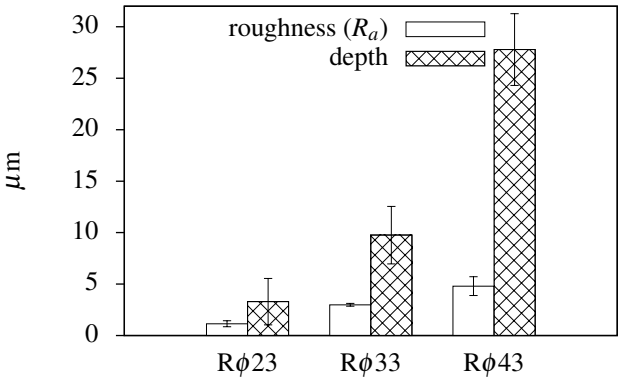

Figure 14 – Optical images of the ablated features for the reproducibility evaluation: a) Rϕ23; b) Rϕ33; and c) Rϕ43.

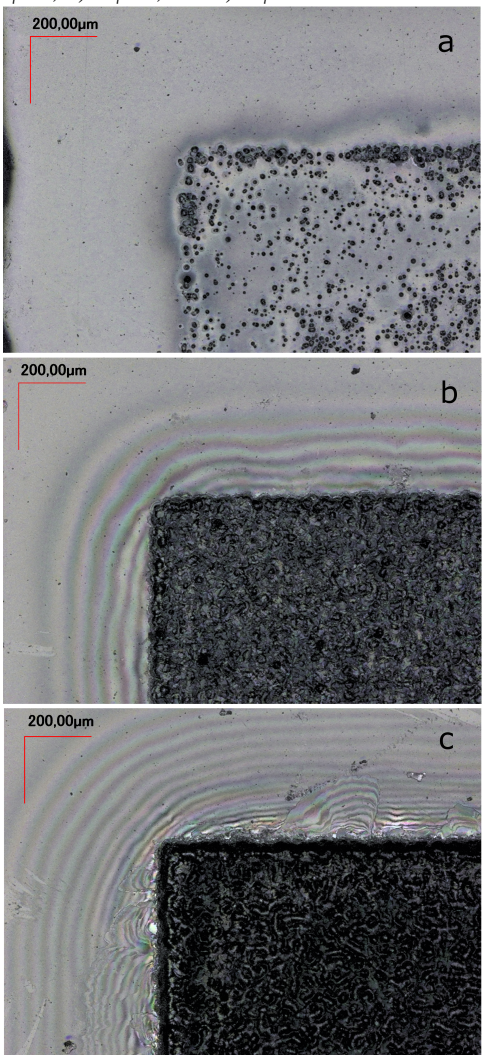

4.3 THRESHOLD INTENSITY AND BEAM RADIUS

The linear relation of D_a^2 and $ln(P_p)$, which would be expectable according to eq. 2.8 is indeed observed (Fig. 15), and allowed the estimation of the focal spot radius (w_e = 23,1 μm) and the threshold ablation fluences for V_s=150 mm/s ($\phi_{v150_{th}}$=19,3 J/cm^2) and for V_s=300 mm/s ($\phi_{v300_{th}}$=16,7 J/cm^2).

Figure 15 – Groove width as function of pulse peak power for scan speeds 150 and 300 mm/s.

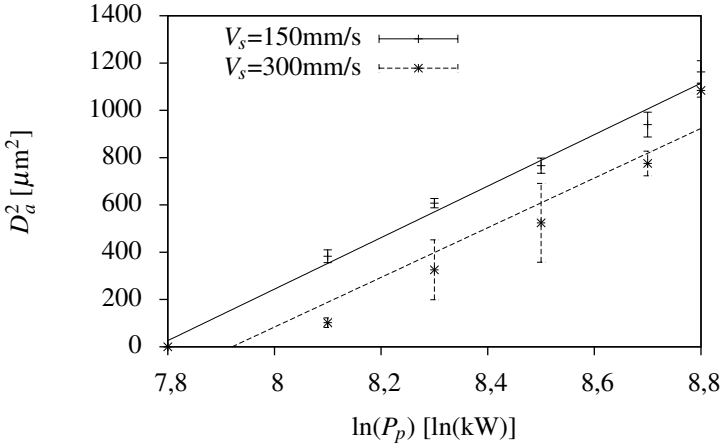

Figure 16 (a) shows the single-pulse ablation depth $h_a(0)$ as a function of beam fluence. It should be noted that the absorption coefficient is affected by the intensity of the beam and the temperatures that the structure comes to. For this reason, eq. 2.10 could not be used to estimate an overall intensity threshold. It allows, nevertheless, to calculate the absorption coefficient for each parameters set based on the single-pulse ablation depth $h_a(0)$, since the intensity values are known. The plot of absorption α vs fluence ϕ is shown in Fig.16(b).

Figure 16 – a) Single pulse removal $h_a(0)$ and b) absorption coefficient α as functions of fluence.

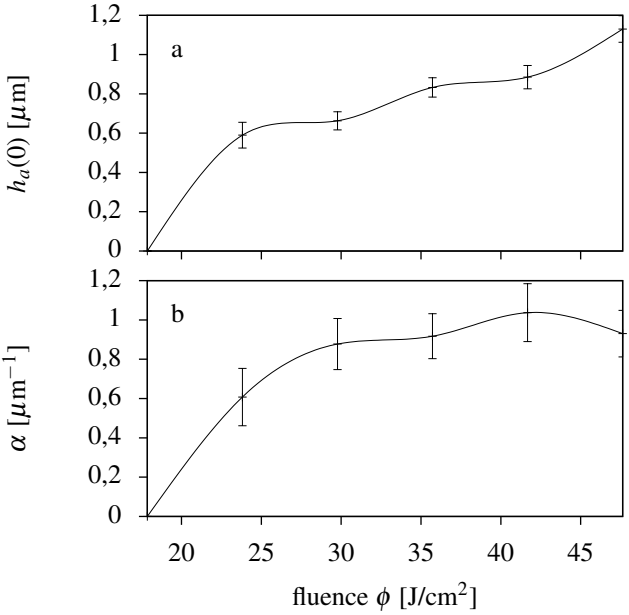

4.4 TRACK DISTANCES

Figs. 17, 18 and 19 show the height profile images for the TDϕ24, TDϕ30 and TDϕ42 sets, respectively. The left region of each image shows the original non-ablated surface, and the right region shows the surface resulting from ablation with different track distances (tracks are on the vertical direction).

Figure 17 – Height profile of ablated area for the TDϕ24 set, with decreasing track distances: a) 16 μm; b) 14 μm; c) 12 μm; d) 10 μm; e) 08 μm and f) 06 μm.

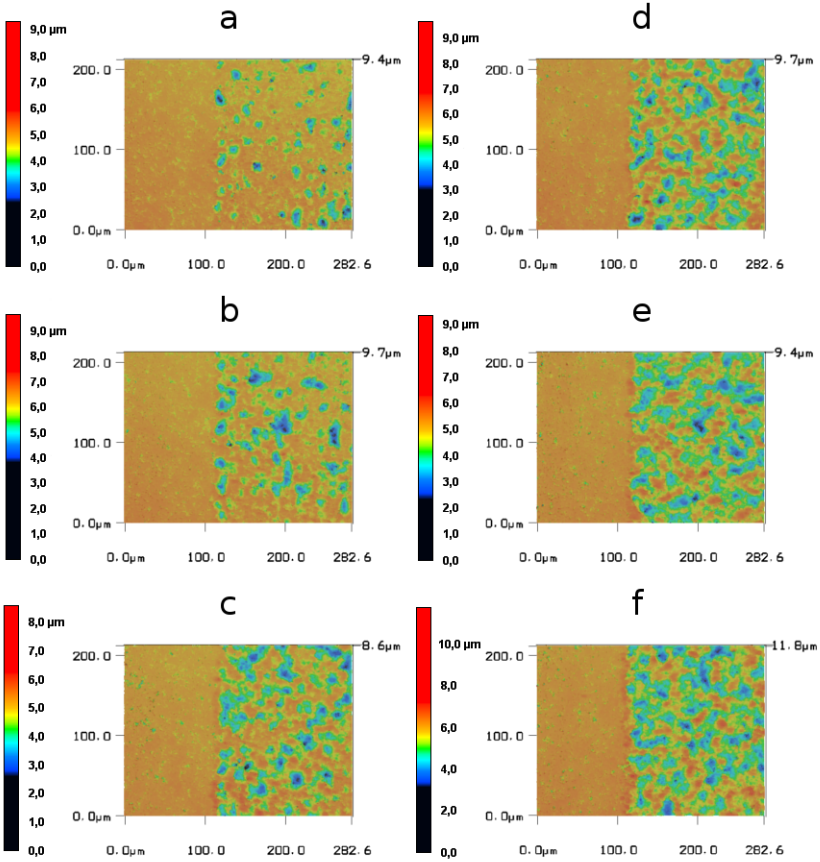

Figure 18 – Height profile of ablated area for the TDϕ30 set, with decreasing track distances: a) 16 μm; b) 14 μm; c) 12 μm; d) 10 μm; e) 08 μm; and f) 06 μm.

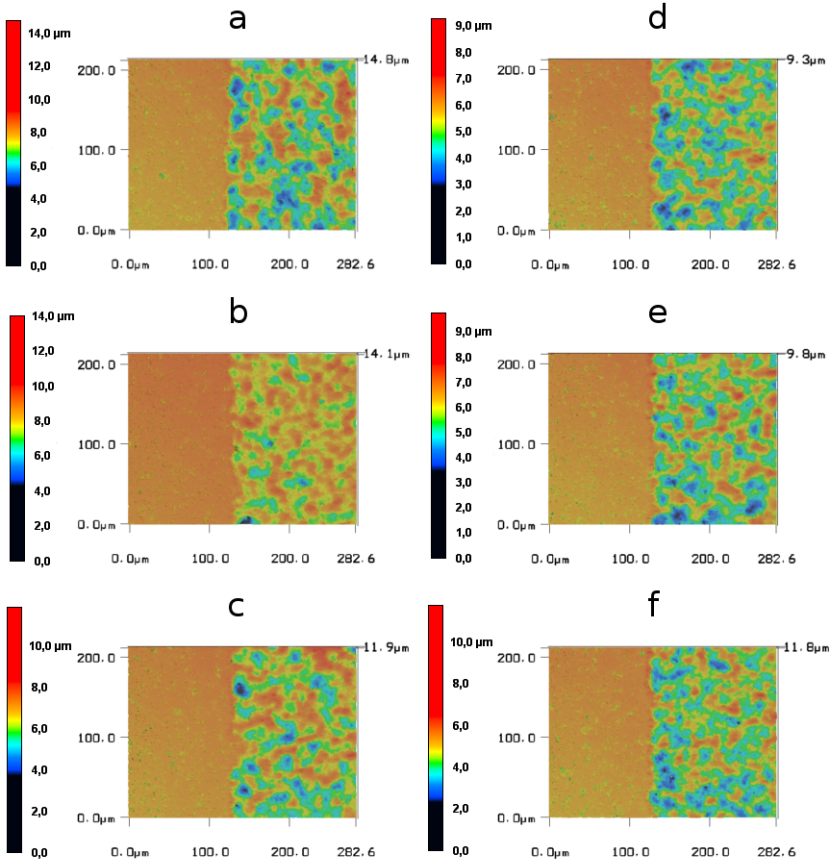

Figure 19 – Height profile of ablated area for the TDϕ42 set, with decreasing track distances: a) 20 μm; b) 18 μm; c) 16 μm; d) 14 μm; e) 12 μm; and f) 10 μm.

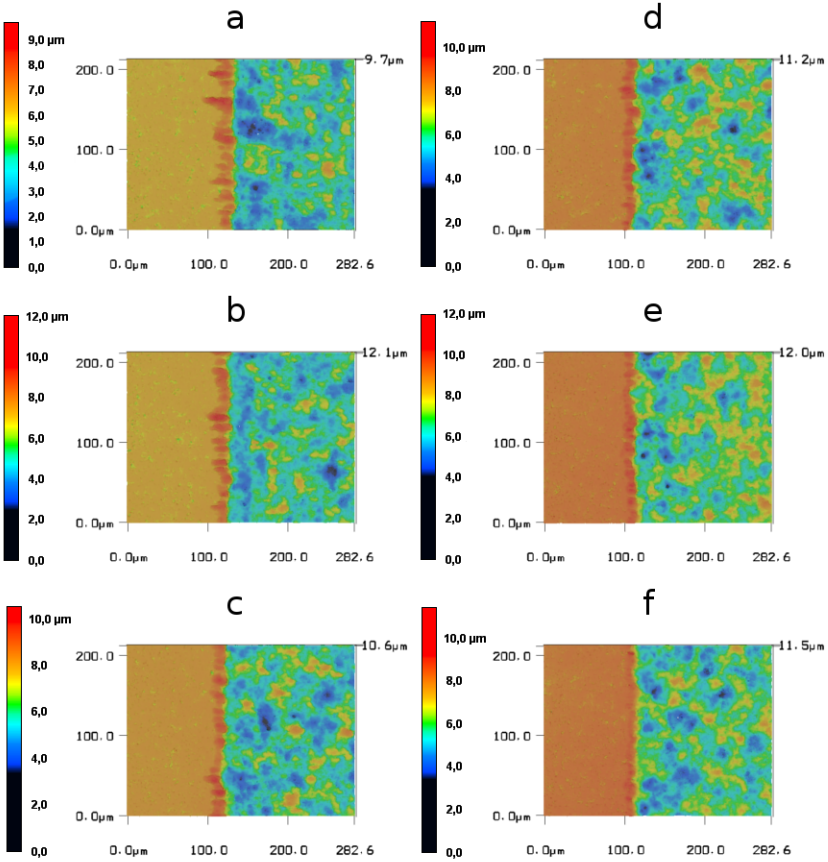

4.5 SCAN SPEEDS

The ablation rate A_r, calculated as the ablated volume divided by the processing time, is plotted as a function of scan speed V_s for three parameters sets in Fig. 20.

Figure 20 – Ablation rate as function of scan speed for SSϕ30; SSϕ36; and SSϕ42.

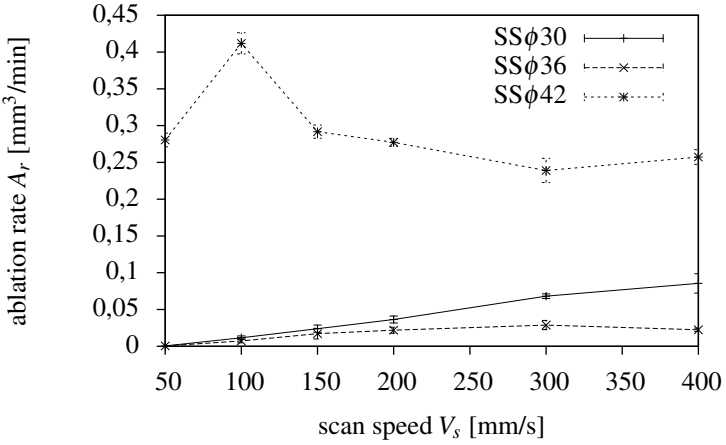

4.6 FRACTURE STRENGTH

The fracture stresses of both the non-ablated and ablated samples had a very good fit to the Weibull distribution, as shown in Fig. 21. A resume of the results is listed on Tab. 8. The relative frequency of defects has been calculated and is shown in Fig. 22.

Table 8 – Weibull modulus and characteristic stress results.

Set name	Wϕ00	Wϕ36	Wϕ42
Mean strength (std. dev.) [MPa]	483(77)	242(15)	142(11)
Determination coefficient R^2	0,9795	0,9565	0,9753
Characteristic strength [MPa]	515	249	146
Weibull modulus	7,4	19,5	16,4

Figure 21 – Weibull fitting for the alumina samples, without ablation (Wϕ00) and ablated with fluences of 36 J/cm^2 (Wϕ36) and 42 J/cm^2 (Wϕ42).

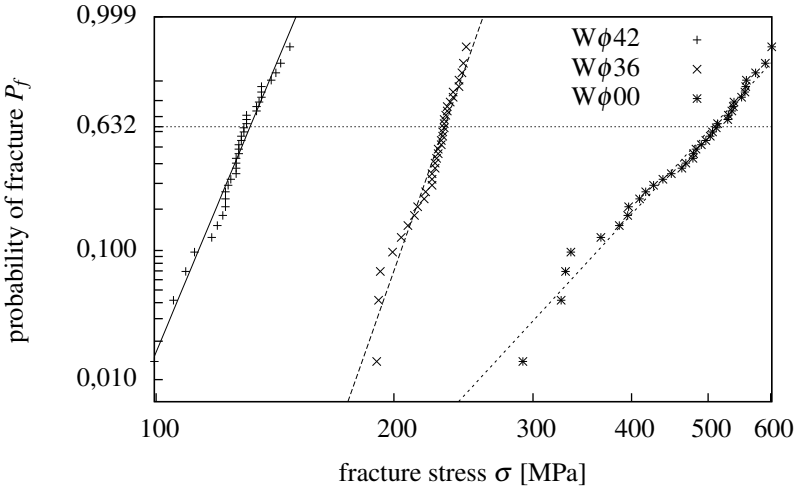

Figure 22 – Frequency distribution density of defect sizes vs defect size for alumina samples without ablation (Wϕ00) and ablated with fluences of 36 J/cm^2 (Wϕ36) and 42 J/cm^2 (Wϕ42).

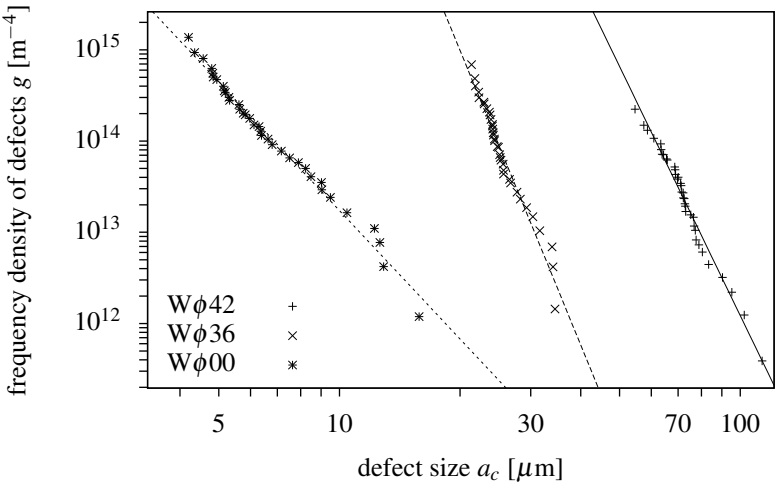

4.7 SURFACE MORPHOLOGY

Both parameter sets used for the strength assessment were also investigated with respect to their surface morphologies, through LSM (Fig. 23) and SEM (Fig. 24)

Figure 23 – LSM surface measurements showing non-ablated (top border) and ablated regions: a) Wϕ36; and b) Wϕ42.

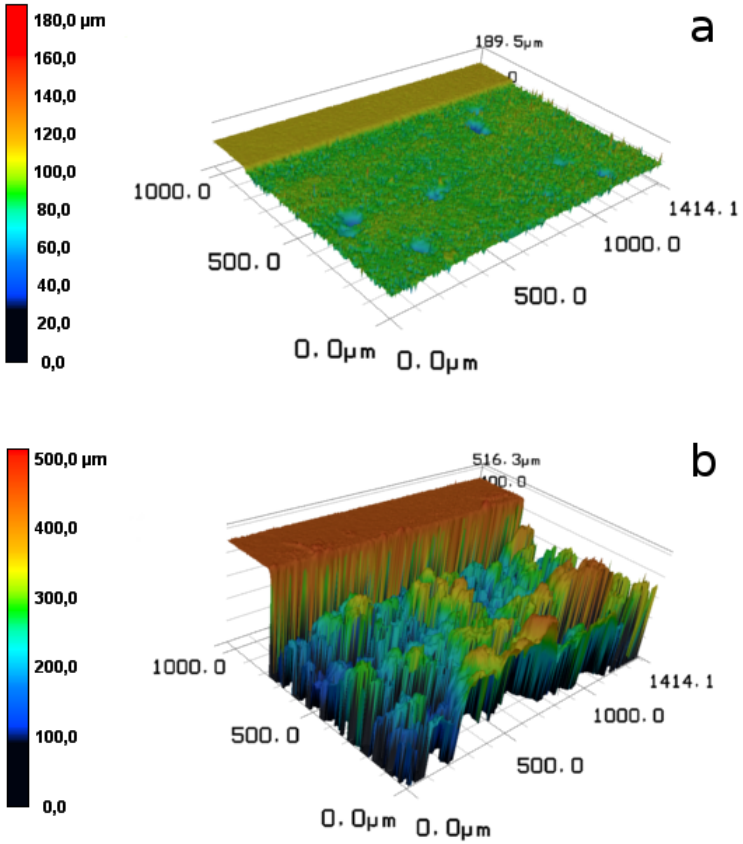

Figure 24 – SEM pictures of Wϕ00, Wϕ36 and Wϕ42 (first, second and third columns, respectively), at increasing magnifications from top down.

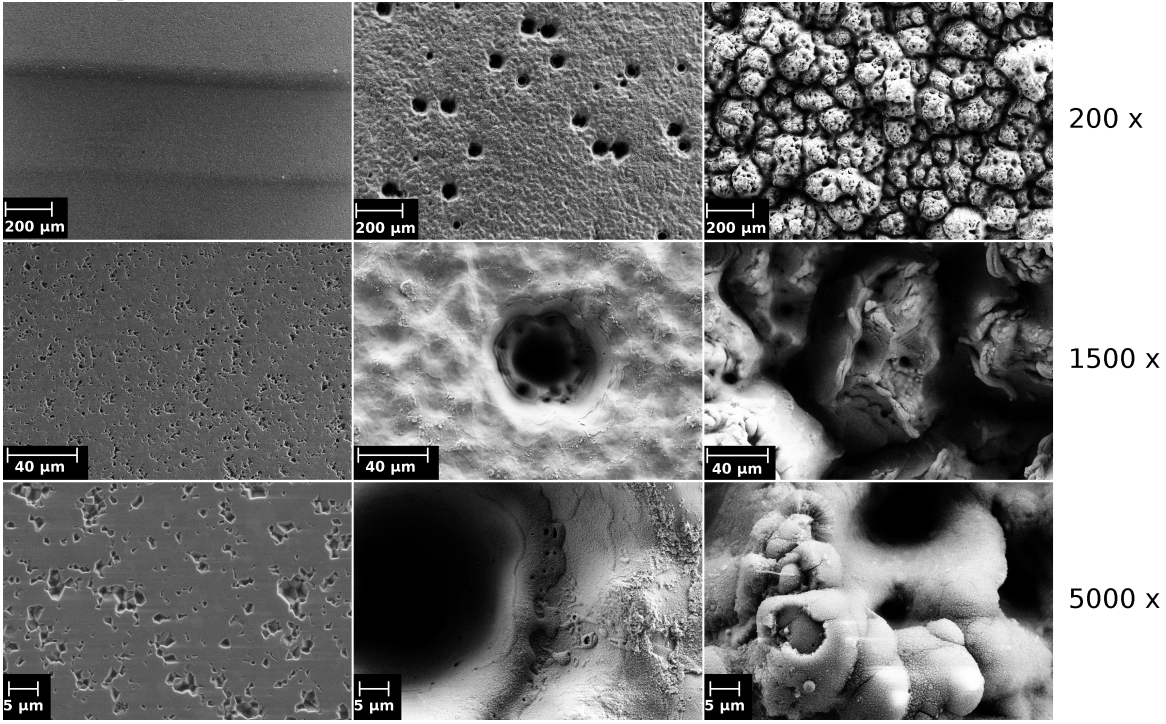

5 DISCUSSION

5.1 MECHANISMS OF REMOVAL

Nanosecond ablation can occur through many mechanisms, depending on material and laser parameters range, and these mechanisms interact and couple themselves (BÄUERLE, 2011); for instance, the excitation energy might be instantaneously transformed into heat, which changes the optical properties of the material and hence the absorbed power. So different models such as thermal, mechanical, photophysical, photochemical and defect allows one to analyse only very specific cases.

The outcomes of most the experiments pointed to ablation by melting and evaporating, with increasing evaporation/melting ratio for increasing fluences. The increase in roughness for higher powers, whose values can be seen in Figs. 12 and 13, is consistent with the findings of Vora et al. (2012), who developed a computational model to understand the influence of single-pulses on the surface finish of alumina for different laser energy densities. The effect is explained as being due to the higher velocity gradient of the molten material, generated by the recoil pressure which increases with energy density, giving higher melt "pile-ups".

Comparing the surface profiles of the track distance experiment, there seems to be a critical distance for the TDϕ30 set (Fig. 18) at 14 μm, where the expelled melt from each line is thrown over the previously ablated line, impairing the process efficacy. This effect of track distance is less pronounced for the TDϕ42 set (Fig. 19), what was attributed to this set's higher evaporation/melting ratio. Track distances of 10 μm and smaller gave very similar surface morphologies independent of the fluence, this being the reason for this value to be adopted for all subsequent tests.

As for the scan speed experiment, the SSϕ42 set (Fig. 20) shows a behaviour that was also reported by Wang et al. (2008). The observed peak at 100 mm/s is justified by the fact that higher speeds result in shallower tracks, hence giving smaller ablation rates, while lower speeds make the tracks too deep, so that the recoil pressure of the vapour phase is not enough to expel the molten material from their bottom. So it resolidifies, impairing the process efficiency. The other sets, of slightly lower fluences, resulted in considerably lower ablation rates, what points different mechanisms or phenomena taking place, as discussed below.

Also when looking to the SEM and LSM pictures (Fig. 24 and Fig. 23, respectively), the kinds of morphologies can be related to the ablation

rate behaviours. While the Wϕ36 set presented a fairly uniform surface, with distinguishable melt pool marks and evenly distributed "holes", the Wϕ42 set gave rise to a highly irregular, rough surface. Measurement of the roughness parameters was not even possible, due to the large non-focusable fraction of the surface. From the lower rates for Wϕ36 set (Fig. 20), combined with the flat morphology of pulse marks and visible melt signs around holes, one can infer that the irradiated energy was not enough to totally overcome the latent heat of vaporization; while the Wϕ42 set's irregular morphology can be credited to turbulence being caused on the melt phase by the vaporizing surface - as suggested by Harimkar and Dahotre (2008) for continuous-wave Nd:YAG treatment of alumina and Lu et al. (2002) for nanosecond ablation of silicon - followed by very fast resolidification that freezes the non-equilibrium structures. Knowles et al. (2007) reported this kind of mechanism for longer (micro- and milliseconds) pulses, and that precise features ($\pm$ 1 μm) were achieved on alumina, without signs of melting, by drilling and cutting with a copper vapour laser (511 and 578 nm wavelength) and 20 ns pulse-width.

The holes observed in the Wϕ36 set may be related to cracks that are formed due to thermal stresses, which expand and spall as consequence of later pulses (WANG; ZENG, 2007). This mechanism sounds reasonable, considering the effect of multiple reflections on the holes' walls (KI; MOHANTY; MAZUMDER, 2002) and noting the molten appearance of the holes' interior and their size, larger than the pulse spots. The marks around these holes were also noteworthy, resembling seemingly linear shock-waves, with well-defined direction changes (Fig. 24). While no proposal of explanation is offered to this effect, it is expected to help give insight into the process mechanisms or provide verification for eventual numerical models regarding plasma dynamics and related shock-wave propagation in other works. In Fig. 14 one can distinguish the effect of shock-waves around the ablated area, whose extents are proportional to the applied laser intensity, and hence to the temperature of the plasma plume, in agreement with Knowles et al. (2007) and Yeo et al. (2012). For the highest intensity, cracks are visible in the borders of the ablated feature. Although the models about laser-ablation plasma formation and behaviour involve complex physics and pose a considerable challenge (AMORUSO et al., 1999), a simple idea of its effect on the overall absorption of the material can be deducted from Fig. 16, which shows a somewhat constant absorption beyond $\approx$ 30 J/cm^2. That can be explained by assuming that the fraction of vapour phase interacting with the beam to create the plasma becomes constant beyond that point.

5.1.1 Threshold fluence

The calculated value for threshold fluence is consistent with previous unsuccessful attempts of ablation with lower fluences, for the threshold and track distance experiments. It must be noted that the estimated values of ϕ_{th} are only valid for the specified sets of frequency and scan speed, as changing these parameters would change the average power output (for the case of frequency) and the pulse overlapping (both frequency and scan speed). The inverse proportionality between scan speed and threshold fluences (Fig. 15) can be explained by the different machining temperatures, which are higher for lower speeds, as pointed by Wang et al. (2008) for nanosecond ablation of Y-TZP ceramics. Also, the threshold fluence in the nanosecond regime is generally higher and not as sharply defined as for ultrashort pulses (BROWN; ARNOLD, 2010), since energy is not so rapidly deposited in the material, giving more time for the excited volume to transfer energy to the surroundings.

This non-sharp threshold fluence could be observed in the reproducibility (Fig. 14) and track distance (Fig. 17) experiments, where the parameter sets of lowest fluence (23 and 24 J/cm^2, respectively) showed irregular ablation behaviour, with non-uniform ablated pulses distribution over the irradiated area. In the graph of the absorption coefficient as function of fluence (Fig. 16), one can note that the mentioned fluences are below the point where it reaches a kind of plateau (J $\approx$ 30 J/cm^2). In all carried experiments, uniform removal was only achieved with fluences higher than that, and it should be taken into account when considering actual applications, that the optimal ablation conditions were achieved with values of fluence ϕ of about 1,5-2ϕ_{th}.

5.2 PARAMETERS TUNING

The lack of fit of the response surface model can be attributed to the mechanisms and phenomena that occur for different levels of fluence, as previously discussed. A curious observation was that both ablation depth and surface roughness, for a specific set of combinations (pump current: 73 %; frequency: 78 kHz, scan speed: 1250 mm/s and track distance: 24 μm) were outliers for both replicates, besides showing a blueish colour in the ablated region (opposed to pale yellow on all others). These points can be recognized by their large deviations in Figs. 11 and 12. The origin of the different behaviour for this set of parameters hasn't been further investigated in the present work.

Translating the laser equipment parameters to the process characteristics, the most pronounced factor regarding ablation depth was found to be the pumping current, and this is justified by the fact that it directly relates to the pulse energy. Increasing frequency, on the contrary, doesn't affect pulse energy because the increase in the average output power is compensated by the decrease in the inter-pulses interval. The overall increase in ablation depth with increasing frequency can, based on the previous discussion, be attributed to the increase in pulse overlapping, as the amount of transferred energy per area is bigger, besides the improvement in process efficiency, as the material has less time to cool between pulses, and taking into account that the ablation threshold is temperature-dependent. The overlapping explanation is also valid for the observed effects of scan speed and track distance. The main effects of the laser parameters on the measured responses (ablation depth and surface roughness) showed similar behaviours to those of Campanelli et al. (2007), for an aluminium-magnesium alloy and a Nd:YVO_4 laser.

5.3 FRACTURE STRENGTH

Tensile residual stresses would be expected from the laser process according to Yeo et al. (2012) study, which found those to be proportional to the irradiated energy density for 50 ns Nd:YAG pulses on Al_2O_3. Indeed, both tested sets, Wϕ36 and Wϕ42, show considerable lower strength values compared to the non treated reference Wϕ00, i.e. 242 and 144 MPa compared to 477 MPa, respectively (Tab. 8). On the other hand, the Weibull modulus increased from 7.4 to 19.5 and 16.4, respectively.

These results indicate that the laser machining did introduce defects larger than the original ones, and these new defects are more homogeneous in size (Fig. 22) than those of the as-polished samples, thereby giving less scattering of the strength. The calculations for defect size assumed volume penny-shaped cracks for the sake of comparison, and a more precise geometry factor could be used if the fracture-originating cracks were identified and characterized through fracture surface analysis. For this reason, and as fracture probably starts from surface defects for the ablated samples, the crack sizes on Fig. 22 must be considered carefully. For the Wϕ42 set, it is very difficult to identify possible fracture-originating sites through the SEM images (Fig. 24), as the regions around melt pillars (in black) could all be taken as cracks. The images of the more homogeneous Wϕ36 set, in their turn, suggest that fracture could be caused by the already mentioned "holes" that are spread through the ablated surface, as they seem to be the largest visible

defects. However, due to the inability to focus on their inner regions, it was not possible to estimate these holes depth.

Studies of the influence of conventional machining on bending strength of Al_2O_3 (FREI; GRATHWOHL, 1993; UEDA; OHNO; SAKAMOTO, 1996) have found the same behaviour of increased Weibull modulus and decreased characteristic stress, with similar values for m (i.e. 14,3 and 18,2) but comparatively higher strengths, even for larger material removal - e.g. a drop from 430 to 296 MPa for $\sim 600\ \mu$m removal, while the observed drop in the present work was from 483 to 142 MPa for $\sim 300\ \mu$m removal (the Wϕ42 set). This can be explained by considering that an increase in the laser intensity brings a series of thermal damaging effects. A possible way of circumventing this problem would be the use of a higher number of removal layers with lower intensities, though that would imply a much lower process efficiency.

5.4 POTENTIAL APPLICATIONS

As mentioned in section 2.2, a relatively high variance of the process is expected due to the nature of the nanosecond ablation removal mechanisms, which rely on vaporization from a melted phase, and are subjected to the plasma influence. The reproducibility experiments showed that it is possible to work within a range of 10 μm of removal for the studied power levels, allowing a choice based on desired removal and roughness.

The very small removal rates, however, associated with the considerable damage caused by the process, make it unable to compete with conventional machining processes. Its advantages of precision, speed and non-contact would probably be better applied for marking and/or engraving applications.

6 CONCLUSION

Laser ablation of alumina with a 120 ns pulsed ytterbium fiber laser has been experimentally analyzed, allowing the individual optimization of each laser parameter, in a sequential way. Two removal regimes were observed, with very distinct ablation rates, surface morphologies and fracture strengths. Nonetheless, the set with the highest removal rate also caused a substantial decrease in the samples strength, suggesting that this kind of laser process may not be the fittest for alumina in load bearing applications, since better results regarding surface quality were already reported elsewhere (KNOWLES et al., 2007), even though the mechanical evaluation for that process analysis is lacking.

Despite the process characterization, because the laser-material interactions are very sensitive to the beam and material characteristics, there is still much work to be carried in future research to achieve a generalized understanding of the process mechanisms. These results are expected to contribute to the development of future technologies as well as provide a basis to validate numerical models to come.

6.1 SUGGESTION FOR FUTURE WORKS

- The ablation depth for experiments with 25 and 50 removal layers were quite distinct, pointing the need for further analysis of this factor;

- The cause for the anomalous behaviour of the parameter combination mentioned on section 5.2 (pump current: 73%; frequency: 78 kHz, scan speed: 1250 mm/s and track distance: 24 μm), regarding its blueish colour and the considerable differences in removal depth and roughness could benefit from further investigation;

- A more detailed analysis for the range of fluences between 36 and 42 J/cm^2 could be carried, possibly defining the turning point of the different observed ablation mechanisms;

- The response surface method could be tried again without the ”track distance” factor and for narrower ranges of the remaining parameters, in the surroundings of the optimized combinations or in the edges of the two mechanisms mentioned in the previous item;

- The damage evaluation could be enhanced by analysing the fracture surfaces of the samples, comparing the size of the fracture-originating defects with those calculated through the Griffith/Irwin criterion;
- The influence of the microstructure (grain size, porosity) of the samples on the process outcomes could be studied and could shed a better light on the underlying mechanisms.

BIBLIOGRAPHY

AMORUSO, S. et al. Characterization of laser-ablation plasmas. **Journal of Physics B: Atomic, Molecular and Optical Physics**, IOP Publishing, v. 32, n. 14, p. R131, 1999.

ASHKENASI, D.; STOIAN, R.; ROSENFELD, A. Single and multiple ultrashort laser pulse ablation threshold of Al2O3 (corundum) at different etch phases. **Applied Surface Science**, Elsevier, v. 154, p. 40–46, 2000.

BÄUERLE, D. **Laser Processing and Chemistry**. [S.l.]: Springer, 2011.

BROWN, M. S.; ARNOLD, C. B. Fundamentals of laser-material interaction and application to multiscal surface modification. In: **Laser Precision Microfabrication**. [S.l.]: Springer, 2010. p. 91–120.

CAMPANELLI, S. et al. Experimental analysis of the laser milling process parameters. **Journal of Materials Processing Technology**, Elsevier, v. 191, n. 1, p. 220–223, 2007.

CHICHKOV, B. et al. Femtosecond, picosecond and nanosecond laser ablation of solids. **Applied Physics A**, Springer, v. 63, n. 2, p. 109–115, 1996.

CHIVEL, Y.; PETRUSHINA, M.; SMUROV, I. Influence of initial micro-porosity of target on material ejection under nanosecond laser pulses. **Applied Surface Science**, Elsevier, v. 254, n. 4, p. 816–820, 2007.

CIRISAN, M. et al. Laser plasma plume structure and dynamics in the ambient air: The early stage of expansion. **Journal of Applied Physics**, v. 109, p. 103301, 2011.

DAHOTRE, N. B.; HARIMKAR, S. P. **Laser Fabrication and Machining of Materials**. [S.l.]: Springer, 2008.

DANZER, R. Some notes on the correlation between fracture and defect statistics: Are Weibull statistics valid for very small specimens? **Journal of the European Ceramic Society**, Elsevier, v. 26, n. 15, p. 3043–3049, Jan 2006.

DEUTSCHES INSTITUT FÜR NORMUNG. **DIN EN 658-3:2002-11**: Hochleistungskeramik - Mechanische Eigenschaften von keramischen Verbundwerkstoffen bei Raumtemperatur - Teil 3: Bestimmung der Biegefestigkeit. Berlin, Germany, nov. 2002.

DEUTSCHES INSTITUT FÜR NORMUNG. **DIN 32540:2012-08**: Laserstrahlabtragen - Thermisches Abtragen mit dem Laserstrahl - Begriffe, Einflussgrossen, Durchfuhrung. Berlin, Germany, ago. 2012.

DUBEY, A. K.; YADAVA, V. Laser beam machining - a review. **International Journal of Machine Tools and Manufacture**, Elsevier, v. 48, n. 6, p. 609–628, 2008.

EICHLER, H. J.; EICHLER, J. **Laser**. [S.l.]: Springer, 2010.

FAN, C.-H.; LONGTIN, J. P. Modeling optical breakdown in dielectrics during ultrafast laser processing. **Applied Optics**, OSA, v. 40, n. 18, p. 3124–3131, Jun 2001.

FREI, H.; GRATHWOHL, G. Microstructure and strength of advanced ceramics after machining. **Ceramics International**, v. 19, n. 2, p. 93–104, 1993.

FU, Z. et al. Experimental study of infrared nanosecond laser ablation of silicon: The multi-pulse enhancement effect. **Applied Surface Science**, Elsevier, v. 256, n. 7, p. 2092–2096, 2010.

GREEN, D. **An Introduction to the Mechanical Properties of Ceramics**. [S.l.]: Cambridge University Press, 1998.

GUSAROV, A. V.; SMUROV, I. Thermal model of nanosecond pulsed laser ablation: Analysis of energy and mass transfer. **Journal of Applied Physics**, AIP, v. 97, n. 1, 2005.

HARIMKAR, S. P.; DAHOTRE, N. B. Characterization of microstructure in laser surface modified alumina ceramic. **Materials Characterization**, Elsevier, v. 59, n. 6, p. 700–707, 2008.

JAHANMIR, S.; RUMULU, M.; KOSHY, P. **Machining of Ceramics and Composites**. [S.l.]: Taylor & Francis, 1999. (Manufacturing Engineering and Materials Processing).

JAYATILAKA, A.; TRUSTRUM, K. Statistical approach to brittle fracture. **Journal of Materials Science**, Kluwer Academic Publishers, v. 12, n. 7, p. 1426–1430, 1977.

JR., E. K.-A. **Principles of Laser Materials Processing (Wiley Series on Processing of Engineering Materials)**. [S.l.]: Wiley, 2009. ISBN 0470177985.

KI, H.; MOHANTY, P. S.; MAZUMDER, J. Multiple reflection and its influence on keyhole evolution. **Journal of Laser Applications**, v. 14, p. 39, 2002.

KIBRIA, G.; DOLOI, B.; BHATTACHARYYA, B. Experimental analysis on Nd:Yag laser micro-turning of alumina ceramic. **The International Journal of Advanced Manufacturing Technology**, Springer, v. 50, n. 5-8, p. 643–650, 2010.

KIBRIA, G.; DOLOI, B.; BHATTACHARYYA, B. Predictive model and process parameters optimization of Nd:Yag laser micro-turning of ceramics. **The International Journal of Advanced Manufacturing Technology**, Springer, v. 65, n. 1-4, p. 213–229, 2013.

KIM, S. H.; SOHN, I.-B.; JEONG, S. Ablation characteristics of aluminum oxide and nitride ceramics during femtosecond laser micromachining. **Applied Surface Science**, Elsevier, v. 255, n. 24, p. 9717–9720, 2009.

KNOWLES, M. et al. Micro-machining of metals, ceramics and polymers using nanosecond lasers. **The International Journal of Advanced Manufacturing Technology**, Springer, v. 33, n. 1-2, p. 95–102, 2007.

LU, Q. et al. Delayed phase explosion during high-power nanosecond laser ablation of silicon. **Applied Physics Letters**, American Institute of Physics (AIP), v. 80, n. 17, p. 3072, 2002.

LUO, Y.-R. **Comprehensive Handbook of Chemical Bond Energies**. [S.l.]: CRC Press, 2010.

MARINESCU; D., I. **Handbook of Advanced Ceramics Machining**. [S.l.]: CRC Press, 2012.

MEIJER, J. et al. Laser machining by short and ultrashort pulses, state of the art and new opportunities in the age of the photons. **CIRP Annals-Manufacturing Technology**, Elsevier, v. 51, n. 2, p. 531–550, 2002.

MORRELL, R. Fracture toughness testing for advanced technical ceramics: internationally agreed good practice. **Advances in Applied Ceramics**, Maney Publishing, v. 105, n. 2, p. 88–98, Apr 2006.

MUNZ, D.; FETT, T. **Ceramics: Mechanical Properties, Failure Behaviour, Materials Selection**. [S.l.]: Springer, 1999.

PHAM, D. et al. Laser milling as a rapid micromanufacturing process. **Proceedings of the Institution of Mechanical Engineers, Part B: Journal of Engineering Manufacture**, Sage Publications, v. 218, n. 1, p. 1–7, 2004.

PHAM, D.; DIMOV, S.; PETKOV, P. Laser milling of ceramic components. **International Journal of Machine Tools and Manufacture**, Elsevier, v. 47, n. 3, p. 618–626, 2007.

QUINN, J. B.; QUINN, G. D. A practical and systematic review of Weibull statistics for reporting strengths of dental materials. **Dental Materials**, Elsevier, v. 26, n. 2, p. 135–147, 2010.

RICHERSON, D. **Modern Ceramic Engineering: Properties, Processing, and Use in Design, Third Edition**. [S.l.]: Taylor & Francis, 2005.

RIEDEL, R.; CHEN, I. **Ceramics Science and Technology, Materials and Properties**. [S.l.]: Wiley, 2011.

SALMANG, H.; SCHOLZE, H. **Keramik**. [S.l.]: Springer, 2007.

SAMANT, A. N.; DAHOTRE, N. B. Differences in physical phenomena governing laser machining of structural ceramics. **Ceramics International**, Elsevier, v. 35, n. 5, p. 2093–2097, 2009.

STEEN, W. M.; MAZUMDER, J. **Laser Material Processing**. [S.l.]: Springer, 2010.

UEDA, T.; OHNO, Y.; SAKAMOTO, S. Superfinishing of fine ceramics. **Journal of the Japan Society for Precision Engineering**, v. 62, n. 7, p. 1014–1018, 1996.

VORA, H. D. et al. Evolution of surface topography in one-dimensional laser machining of structural alumina. **Journal of the European Ceramic Society**, Elsevier, 2012.

WACHTMAN, J.; CANNON, W.; MATTHEWSON, J. **Mechanical Properties of Ceramics**. [S.l.]: Wiley, 2009.

WANG, C.; ZENG, X. Study of laser carving three-dimensional structures on ceramics: Quality controlling and mechanisms. **Optics & Laser Technology**, Elsevier, v. 39, n. 7, p. 1400–1405, 2007.

WANG, X. et al. Optimized nanosecond pulsed laser micromachining of Y-TZP ceramics. **Journal of the American Ceramic Society**, Wiley Online Library, v. 91, n. 2, p. 391–397, 2008.

WU, J. et al. Infrared nanosecond laser-metal ablation in atmosphere: Initial plasma during laser pulse and further expansion. **Applied Physics Letters**, v. 102, p. 164104, 2013.

YAN, Y. et al. Experimental and theoretical investigation of fibre laser crack-free cutting of thick-section alumina. **International Journal of Machine Tools and Manufacture**, Elsevier, v. 51, n. 12, p. 859–870, 2011.

YAO, W. et al. Grain size dependence of fracture toughness for fine grained alumina. **Scripta Materialia**, Elsevier, v. 65, n. 2, p. 143–146, Jul 2011.

YEO, S. et al. Study of residual stress and surface morphology changes in Al2O3 induced by Nd:Yag laser irradiation. **Journal of materials engineering and performance**, Springer, v. 21, n. 1, p. 137–142, 2012.

ZHOU, Y. et al. Physical mechanism of silicon ablation with long nanosecond laser pulses at 1064nm through time-resolved observation. **Applied Surface Science**, Elsevier, v. 257, n. 7, p. 2886–2890, 2011.